九州大学学術情報リポジトリ
Kyushu University Institutional Repository

# A Computational Study on Thermal and Sustainability Analysis of Solar Air Heater with S and Airfoil Tabulators

Sharma, Sachin
Department of Mechanical Engineering, SOAE, UPES

Maithani, Rajesh
Department of Mechanical Engineering, SOAE, UPES

https://doi.org/10.5109/7172283

出版情報：Evergreen. 11 (1), pp.295-305, 2024-03. Interdisciplinary Graduate School of Engineering Sciences, Kyushu University, Japan
バージョン：
権利関係：Creative Commons Attribution 4.0 International

KYUSHU UNIVERSITY

# A Computational Study on Thermal and Sustainability Analysis of Solar Air Heater with S and Airfoil Tabulators

Sachin Sharma, Rajesh Maithani*

Department of Mechanical Engineering, SOAE, UPES, Dehradun, Uttarakhand, 248007, India.

*Author to whom correspondence should be addressed:
E-mail: rmaithani@ddn.upes.ac.in

(Received November 3, 2023: Revised January 17, 2024: Accepted February 6, 2024)

**Abstract**: The solar air heater (SAH) harnesses solar energy and finds widespread application in various contexts, including drying agricultural products, heating spaces in buildings, etc. However, the viability of SAH has a problematic issue due to its low performance, which limits its applicability in actual applications. In this work, two distinct novel turbulators; namely, S-shape and Airfoil (NACA0018) turbulator have designed to take advantage of their flow structures to get enhanced performance of SAHs. The thermal analysis of rectangular SAH with a combination of S-shape and Airfoil (NACA0018) shape turbulators performed numerically. The operating and geometric parameters are : relative pitch (P/e) varied from 8 to14, angle of attack (α) varied from 0°-45°, and Reynolds number (Re) varied from 4000-16000. Both heat transfer and friction factor characteristics of SAH with turbulators show a significant improvement over smooth SAH. The maximum value of thermos-hydraulic performance is 2.21 which has been achieved at P/e=12, Re=12000 and α=30º. The exergetic analysis was also conducted, yielding a maximum exergetic efficiency of 2.25%.

Keywords: Rectangular Channel; S-shape and Airfoil turbulators; CFD; Thermo-hydraulic performance; Exergetic Performance

## 1. Introduction

The scarcity of diminishing non-renewable energy resources leads to higher utilization of renewable energy resources. Among all the available substitutes, solar energy is a promising source to fulfil energy requirements[1)2)]. It is well-thought-out as the most prominent renewable energy source, owing to its highly prospective availability and environment-friendly nature. Solar energy is used for drying crops[3)], curing industrial products, and heating applications by converting the abundant[4)] source into thermal energy[5)].

Rectangular channel SAHs are promising equipment for harnessing solar power for various uses because of their minimal requirement of material and cost. However, efficiency is reduced because of the poor convective heat transmission between the absorber plate and the surrounding air. Also, uneven heat transfer distribution on side walls leads to performance deterioration of the channel[6)]. Numerous factors like length and depth of the collector, absorber type, cover plate, flow rate etc.[7)8-11)] affect the efficiency of the rectangular channel. The introduction of turbulence in the flow of air increases the convective coefficient[12)] and increases friction to flow, increasing pumping power to meet the flow rate. To augment the turbulence, various turbulators in the flow have been introduced, viz. ribs[13)] baffles[14)15,16)17)] fins[18)19)],jet-impingement[20)21)], perforations[22)], vortex generators[23)] etc. Studies have been further extended with different flow arrangements like parallel, counter flow, recycle flow, etc. Experimentally, Singh et. Al[24)] performed the thermal analysis of a SAH rectangular duct with several arc obstructions on the heated plate. The Nu was increased to 5.07, and the flow friction was reduced by 3.71% compared to smooth ducts. For optimum improvement, aim for a Re of 22300, W/w of 5.0, e/D of 0.045, P/e of 8, and α of 0.667.

Flow through an air heater with dimpled barriers arranged in a V pattern has been experimentally studied to determine Nu and f. Number of refractions per unit area was between 5000 and 17000 by Kumar et al.[25)]. Webb and Eckert[26)] suggested an overall enhancement parameter that considers both hydrodynamic and thermal performance simultaneously. Kumar et al.[27)] conducted tests on a rectangular SAH duct, roughening the heated absorber plate with S-shaped ribs and maintaining an aspect ratio of 12. Wang et al.[28)] performed experiments with several S-shaped ribs with gap roughness on the SAH heated wall.

Luan and Phu[29)] experimentally determined relationships between the Nu and f for an incline baffled solar air heater. The baffles slanted from 0 degrees to 2

hundred and eighty degrees while keeping the pitch the same. When comparing anticipated and experimental values, the Nusselt number's error was 6% and the friction factor's error was 8.3%. At a baffle angle of 0 degrees, the collector's exergetic efficiency is at its lowest. Choose baffle angles between 600 and 1200 for maximum efficiency. Hu et al.[30] tested and calculated baffle-type solar collector thermal performance. There were a total of four different collector models put through their paces under three distinct scenarios. Rearranging baffles and narrowing the first chamber is a fresh approach. The first chamber's width greatly affected the collector's thermal efficiency but not the pressure drop. The narrowing model was not scale-sensitive, thermal efficiency increased from 9.73 per cent to 16.10 per cent, and the system is adaptable. Bensaci[31] positioned SAH baffles experimentally and numerically. Reynolds numbers ranged from 2370 to 8340. Four models baffle position in the second half (50 per cent up), first half (50 per cent down), centre (50 per cent middle), and all in the channel (100 per cent) have been studied. The maximum Nusselt number was 8340 at 100% position. Due to lower friction, thermo-hydraulic performance is highest at 50% down case. Afshari et al.[32] analyzed the design and positioning of turbulators in a cheap tube-type SAH using both experiments and simulations (TSAH). Numerical analysis of the SAH with a simple structure has been performed in FLUENT for complicated geometries. The thermal efficiency of turbulators was improved by 72.41 per cent after some adjustments were made to them. Sharma and Maithani[33] performed experimental on impinging jets to enhance the thermal performance of solar air heater. The exergy analysis has already been performed and results reflected that novel v pattern protrusions and impinging jets have improved thermal performance significantly. Moussaoui et al[34] performed experimental analysis on drying kinetics under controlled environment. Apart from that the experiments were performed to measure the biogas production from waste food. The results reflected that drying kinetics and biogas production vary inversely to each other. In addition to these experimental investigations, many scholars have used numerical analysis to foretell a solar air heater's efficiency (Jin et al.[35] and Singh et al.[36]. Sivakandhan et al.[37] analyzed the hybrid duct with rectangular and triangular ducts roughened with inclined ribs. Singh et al.[38] contrasted several broken and square-shaped ribs with roughened ducts with flat plate duct solar air heater. Square wave-shaped and numerous broken ribs achieve maximum thermal increments of 2.50 and 3.24 times, respectively. While 3.92- and 3.85-times pumping power penalties were received. Yadav and Bhagoria[39] calculated SAH performance with equilateral triangular-sectioned ribs. Twelve roughness configurations with Reynold values from 3800-18000 were examined. P/e ranged from 7.14–35.71 and e/d from 0.021–0.042. S.K. Jain et al.[40] have been quantitatively tested for the thermal efficiency using a V-shaped perforated baffled SAH. Researchers have tested the effect of several roughness factors, including e/H from 0.3 to 0.6, Re from 4000 to 18,000, a close pitch ratio of 6 to 23, a constant open area ratio of 23 per cent, and an angle of attack from 60 degrees. At an equivalent height of obstruction of 0.4, the best thermohydraulic performance value was 2.224. Y.M. Patel et al.[41] using a computer model, researchers have examined how the NACA0040 ribs function as turbulators in a SAH.

The literature review has shown that turbulators of different shapes and sizes have been used on the heated surface of the solar air heater[42-45]. These turbulators increase both Nu and f inside the rectangular channels. These turbulators substantially increase the friction factor. This could be one of the major drawbacks of turbulators. In the present work, a novel smooth shape NACA0018 obstacle with a S-shape turbulator have been used; furthermore, in the open literature, not much comprehensive research has been reported that could state the combined effect of these two turbulators on the performance of the solar air heater. The impact of α, P/e and Re with fixed $e/D_h$ has been studied through ANSYS 19.3 and presented.

## 2. Numerical Analysis

In the present work, the numerical analysis to analyze the performance of the solar air heater has been performed using a computational fluid dynamics approach (CFD). The CFD analysis has been performed using the academic version of ANSYS 19.3 R3. The absorber surface of SAH has S-shaped and Airfoil-NACA0018 turbulators. The computational domain is displayed in Fig. 1(a) with the geometry of the turbulator elements. The dimensions of the SAH are taken as per ASHRAE standards[46]. In the NACA0018 airfoil series, 00 demonstrates that it has zero camber and 18 shows that the airfoil has an 18 percent thickness to the chord length proportion[47]. The absorber plate is subjected to a steady heat flow of 1000 $W/m^2$. The insulation and smoothness of the remaining three sides of the channel are maintained.

The following assumptions are considered while performing simulations:

a) The fluid flow is turbulent and incompressible in the computational domain.

b) The working fluid is air and enters the channel at ambient temperature (300K).

c) No slip conditions on the boundary.

d) Heat transfer by radiation is neglected.

The operating and geometrical parameters are mentioned in Table 1.

Table 1. Operating and Geometrical parameters

| S.No. | Parameter | Range/Units |
|---|---|---|
| **Fixed** | | |
| 1 | Airfoil | NACA0018 (L=100mm, W=18 mm) |

| | | |
|---|---|---|
| 2 | S-Shape | L=100 mm, W= 18 mm |
| 3. | Relative height (e/H) | 0.5 |
| 4 | Hydraulic Diameter ($D_h$) | 54.54 mm |
| **Geometric Parameters** | | |
| 1 | Relative pitch(P/e) | 8,10,12,14 |
| 2 | Angle of attack (α) | 0°,15°,30°,45° |
| 3 | Reynolds Number (Re) | 4000-16000 |

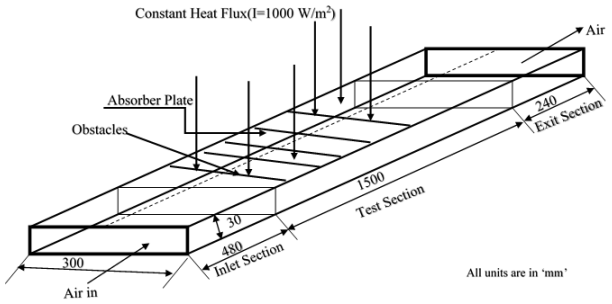


(a)

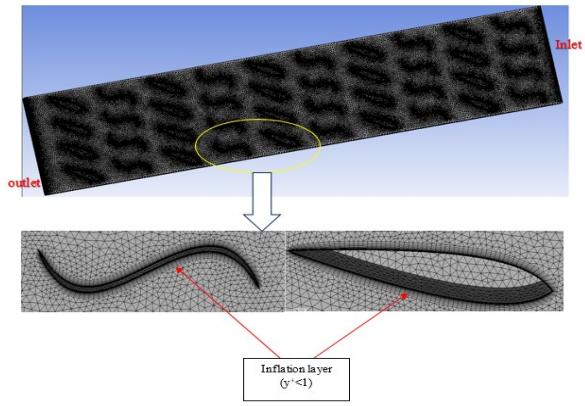


(b)

**Fig. 1(a):** Computational domain **(b)** Meshing

## 2.1 Governing Equations

Incompressible steady-state flow is represented by the following set of governing equations[48,49]:

Continuity Equation: $\frac{\partial(\rho u_j)}{\partial x_j} = 0$ (1)

Momentum Equation: $\frac{\partial(\rho u_i u_j)}{\partial x_j} + \frac{\partial p}{\partial x_i} = \frac{\partial}{\partial x_j}\left(\mu\left[\frac{\partial u_i}{\partial x_j} + \frac{\partial u_j}{\partial x_i}\right]\right) + \frac{\partial}{\partial x_j}\left(\mu_t\left[\frac{\partial u_i}{\partial x_j} + \frac{\partial u_j}{\partial x_i}\right]\right)$ (2)

Energy Equation: $\frac{\partial(\rho u_j T)}{\partial x_i} - \frac{\partial}{\partial x_j}\left(\frac{\partial T}{\partial x_j}(\Gamma + \Gamma_t)\right) = 0$ (3)

## 2.2 Mesh Generation

The finite volume technique (FVM) has been considered to discretize the fluid domain. A fine mesh has been created by providing an inflation layer at the surface to capture the flow vortices near the wall as shown in Fig 1(b). The dimensionless wall distance defines the distance between the first element and the solid boundary $y^+$and which has been kept less than one near the wall. The values of $y^+$ have been varied while meshing various domains. Tetrahedral mesh elements have been used for meshing; the minimum mesh size is 0.0491 mm, and the maximum mesh size is 0.16 mm. The mesh size has been varied to keep the $y^+$ value within the range of 1-5[50].

The governing equations are discretized using an upwind second-order discretization technique, with a criterion of convergence of the order of $10^{-6}$ for the different equations. The $Nu_r$ is calculated for a constant Re of 12000 using a coarse and system-generated mesh. The mesh has been then made finer for the subsequent investigation and $Nu_r$ is again calculated on the same $Re$. It has been observed that after 2812479 elements, $Nu_r$ variation is less than 1%. Thus, 2812479 elements have been taken for detailed investigations. Table 2 illustrates the variation of $Nu_r$ with the number of grid elements.

Table 2. $Nu_r$ variations with mesh elements

| S.No | Number of Elements | Nusselt number ($Nu_r$) | % increment |
|---|---|---|---|
| 1 | 10,00,000 | 73.77 | NA |
| 2 | 15,00,000 | 75.55 | 2.356 |
| 3 | 20,00,000 | 76.78 | 1.602 |
| 4 | 25,00,000 | 77.4 | 0.801 |
| 5 | 28,00,000 | 77.9 | 0.642 |
| **6** | **28,12,479** | **78.25** | **0.447** |
| 7 | 28,50,000 | 78.28 | 0.038 |
| 8 | 29,00,000 | 78.29 | 0.026 |

## 2.3 Boundary Conditions

The steady conditions imply incompressibility and constant density of the fluid flowing inside the channel. Table 3 demonstrates the boundary conditions on various boundaries, i.e., inlet, outlet, absorber plate and walls. Velocity at the inlet has been calculated from Reynolds Number ($Re$). Pressure has been taken as zero gauges on

the outlet face.

Four turbulence models named Shear Stress Transport (SST) k-ω, RNG-Renormalization group k-ε model, Realizable k-ε, and Standard k-ε have been tested for the smooth channel. The SST k-ω model has been selected because the results have less deviation from Dittus Boelter Equation (Eq. 4) and Gnielinski Equation (Eq. 5).

Table 3. Boundary conditions for simulations

| S.No. | Boundary Type | Condition | Values |
|---|---|---|---|
| 1 | Air inlet | Inlet Velocity<br>Temperature | 1.06 -4.26 m/sec.<br>300 K(fixed) |
| 2 | Air Outlet | Pressure | Zero, bar |
| 3 | Heated wall | No Slip | Heat Flux-1000 W/m$^2$ |
| 4 | Adiabatic wall | No Slip | NIL |

### 2.4 Validation test

The simulations have been performed for the smooth channel over Re ranging from 4,000 to 16,000. The obtained results of $Nu_s$ are validated by comparing it with the values determined by Dittus Boelter Equation (Eq.4), Gnielinski Equation (Eq.5), and available experimental results.

Dittus Boelter Equation[51] : $Nu_s = 0.023 \times Re^{0.8} Pr^{0.4}$ (4)

Gnielinski Equation:

$$Nu_s = \frac{\left(\frac{f}{8}\right)(Re-1000)Pr}{1+12.7\left(\frac{f}{8}\right)^{1/2}\left(\left(Pr^{2/3}\right)-1\right)} \quad (5)$$

Where, $f = (0.79 \ln Re - 1.64)^{-2}$, for 3000<Re<5×10$^6$

Similarly, the $f_s$ values of the without rib channel are related with the $f_s$ values of Blasius Equation (Eq.6), Petukov Equation (Eq.7).

Blasius Equation[51]: $f_s = 0.316 \times Re^{-0.25}$ (6)

Petukov Equation: $f_s = (0.79 \ln Re - 1.64)^{-2}$ for 3000<Re<5×10$^6$ (7)

The simulation results of $Nu_s$ and $f_s$ as a function of Re have been represented in Fig. 2. The $\pm 5\%$ deviation has been observed for $Nu_s$ whereas $\pm 4\%$ deviation for $f_s$.

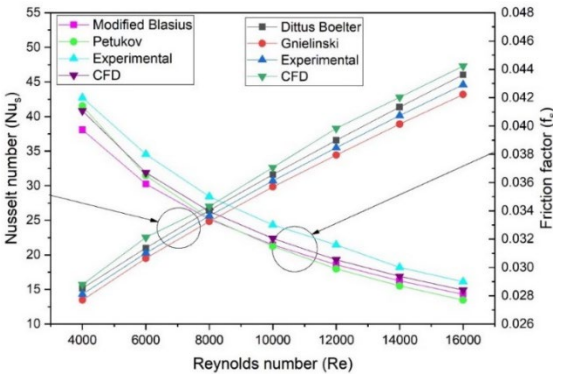


**Fig. 2:** Comparison of $Nu_s$ and $f_s$ with CFD

## 3. Exergy analysis

The parameters for external and internal exergy losses have been based on the second rule of thermodynamics, which was proposed by [52,53].

The several types of energy loss are as follows:

a) Exergy losses in optics($EX_{L,opt}$).

b) Due to heat transmission between SAH components and the outside world, there is an exergy loss($EX_{L,HT}$).

c) Exergy lost due to solar radiation being soaked up by the heated wall($EX_{L,Irr}$).

d) This exergy loss is caused by the fluid's and the absorber plate's different temperature ($EX_{L,FHT}$).

e) Exergy dissipation along the flow route because of fluid friction($EX_{L,Fri}$).

### 3.1 Exergetic Efficiency

The following equations determine solar air heater (SAH) exergetic efficiency ($\eta_{EX}$) [54]:

$$\eta_{EX} = 1 - \frac{\sum EX_{L,Total}}{\sum EX_{IN}} \quad (17)$$

Where, $\sum EX_{L,Total}$ is varied exergy loss parameters.

$\sum EX_{IN}$ is the exergy inlet.

The following equation calculates exergy inlet:

$$\sum EX_{IN} = IA_p\left[1 - \frac{4}{3}\left(\frac{T_a}{T_{Sun}}\right) + \frac{1}{3}\left(\frac{T_a}{T_{Sun}}\right)^4\right] \quad (18)$$

$T_{sun}$=4778 K.

Exergy loss components:

$$\sum EX_{L,Total} = EX_{L,opt} + EX_{L,HT} + EX_{L,Irr} + EX_{L,FHT} + EX_{L,Fri} \quad (19)$$

Eq. 20 calculates the exergy losses:

a) This equation calculates optical loss:

$$EX_{L,opt} = IA_p(1 - \alpha_p\tau_g)\left[1 - \frac{4}{3}\left(\frac{T_a}{T_{Sun}}\right) + \frac{1}{3}\left(\frac{T_a}{T_{Sun}}\right)^4\right] \quad (20)$$

$\alpha_p\tau_g = 0.88$

The following equation calculates SAH component-environment heat transmission exergy loss:

$$EX_{L,HT} = U_L A_p (T_p - T_a)\left[1 - \frac{T_a}{T_p}\right] \quad (21)$$

Where, $U_L = U_t + U_e + U_b$; (22)

$U_L$= Total loss, $U_t$= Transmission loss, Ue= Edge loss, $U_b$= Bottom loss,

b) The following equation calculates the absorber plate's exergy loss from solar irradiation absorption:

$$EX_{L,Irr} = IA_p\alpha_p\tau_g\left[1 - \frac{4}{3}\left(\frac{T_a}{T_{Sun}}\right) + \frac{1}{3}\left(\frac{T_a}{T_{Sun}}\right)^4 - \left(1 - \frac{T_a}{T_p}\right)\right] \quad (23)$$

c) The following equation calculates exergy destruction due to finite temperature difference between fluid and absorber plate:

$$EX_{L,FHT} = IA_p\eta_{th}T_a\left[\left(\frac{1}{T_{sa}}\right) - \left(\frac{1}{T_p}\right)\right] \quad (24)$$

d) The following equation calculates fluid friction exergy loss along the flow route:

$$EX_{L,Fri} = \frac{T_a\dot{m}\Delta P_D}{\rho_a T_{sa}} \quad (25)$$

## 4. Results and Discussion

The $Nu_r$ and $f_r$ of rectangular channel roughened with a S-shape and Airfoil (NACA0018) turbulators are evaluated based on computational data collected for various geometrical and operational parameters. Then, the computed values of $Nu_r$ & $f_r$ have been compared with $Nu_s$& $f_s$ respectively under similar operating conditions.

### 4.1 Heat transfer

The effect of $\alpha$ on $Nu_r/Nu_s$ by varying the operational range of $Re$ from 4000 to 16000, is portrayed in Fig. 3(a) using S-shape and NACA0018 roughness. The value of other geometrical parameters has been kept constant, viz $e/D_h$ at 0.22 and $P/e$ at 12. The $\alpha$ is taken as 0°, 15°, 30° and 45°. A monotonous increase in the value of $Nu_r$ has been noticed with the increase in $Re$ for all selected values of $Re$. The value of $Nu_r$ has been noticed to increase with an increase in $\alpha$ from 0° to 30° and the maximum enhancement in $Nu_r$ is obtained at $\alpha = 30°$ and after that, with any increase in $\alpha$, the value of $Nu_r$ decreases. The possible cause for this enhancement is that at $\alpha = 0°$; the roughness shape is parallel to the direction of fluid flow and at $\alpha = 45°$, it is much more perpendicular. At an angle of $\alpha = 30°$, the secondary flow produced by the S-shape has been found to have a higher intensity of turbulence due to strong vortices generation at the curved surfaces, which eliminates the hot zones in the trailing areas of flow, as evident in the velocity pattern over the turbulators in Fig. 3(b).

Figure 3(c) has been plotted to analyse the effect of $P/e$ of the S-shape and NACA0018 roughness on $Nu_r/Nu_s$ generated for the varying range of $Re$ from 4000-16000 and keeping other geometric parameters constant viz. $e/D_h$ at 0.22 while $\alpha$ at 30°. Figure 3(c) discloses that the $Nu_r$ rises with a rise in the value of $P/e$ from 8 to 12, and after that the $Nu_r$ reductions as $P/e$ is improved beyond the value of 8. The likely reason for maximum $Nu_r$ at $P/e = 12$ is that at a lower pitch, the turbulence created by the leading array of roughness encounters the trailing roughness array. As the $P/e$ value is increased up to 12, the secondary flow and the vortices get adequate space to produce the turbulence a; hence, a larger area encounters the boundary layer breakdown, consequential in better heat transfer. Any increase in the $P/e$ beyond 12 decreases the number of rows attached on the test surface; thus, the number of turbulent promoters reduces, reducing the turbulence. The turbulent fluid now reattaches near the NACA0018 shape and resulting heat transfer augmentation. Figure 4(a-c) shows the temperature variation at different sections of roughened channel, whereas Fig. 4(d) represents the temperature contours along the shape.

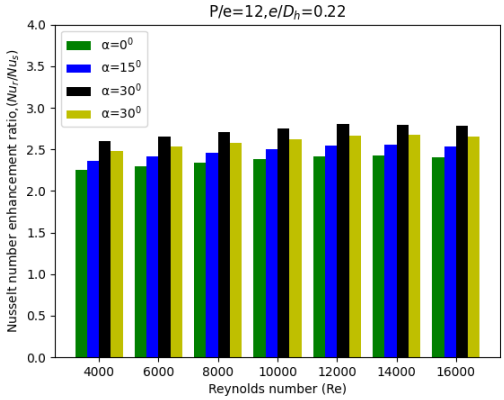


**Fig. 3(a):** Effect of $\alpha$ on $Nu_r/Nu_s$

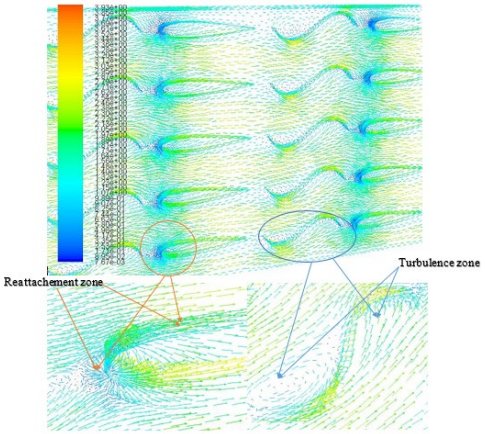


**Fig. 3(b):** Velocity contours at Re=12000 (e/Dh=0.22, P/e=12 and α=30⁰)

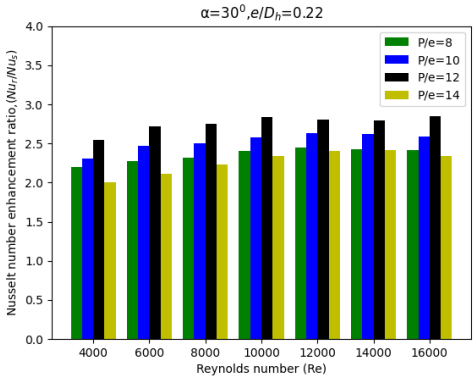


**Fig. 3(c):** Effect of $P/e$ on $Nu_r/Nu_s$

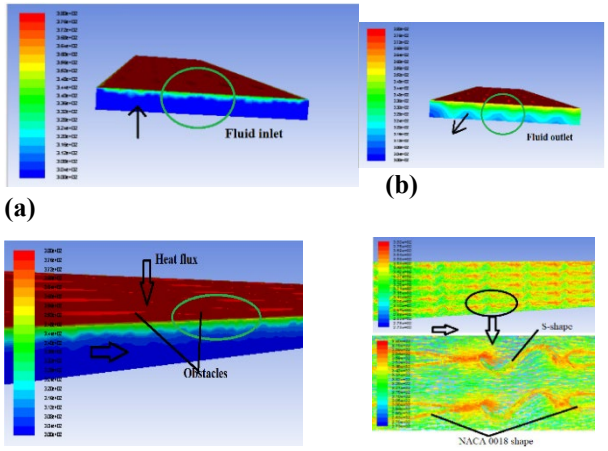


**Fig. 4:** Temperature profile a) Inlet b) Outlet c) Along the length d) Contours along shapes at Re=12000(e/Dh=0.22, P/e=12 and α=30$^0$).

### 4.2 Friction Factor

The effect of $\alpha$ on $f_r/f_s$ at a different operating range of $Re$ from 4000 to 16000 is represented in Fig. 5(a), and the other geometrical parameters are kept constant viz. $P/e$ at 12 and $e/D_h$ at 0.22. The increment in friction factor due to turbulators over friction factor of the smooth surface by varying angle of attack.

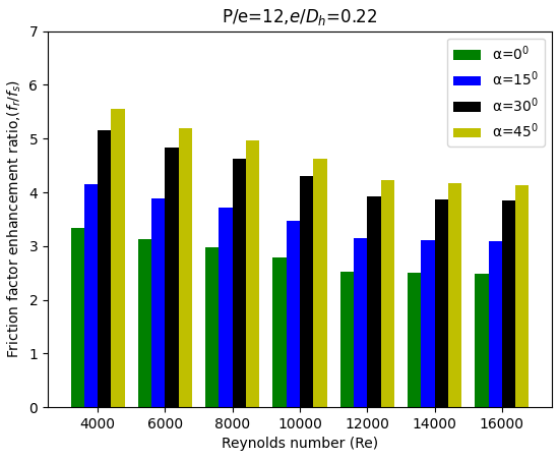


**Fig. 5(a):** Effect of $\alpha$ on $f_r/f_s$

The $\alpha$ has been varied as $0^0$, 15°, 30° and 45°, respectively, and it is observed that the $f_r$ increases monotonously with an increase in $Re$ for the entire range. The value of $f_r$ has been noticed to continuously increase with an increase in $\alpha$ from 0° to 45° and the maximum enhancement in $f_r$ has been obtained at $\alpha = 45°$. The augmentation in $f_r$ has been observed because by increasing the $\alpha$ from 0° to 45°, the alignment of baffles is nearly perpendicular to the direction of the fluid flow.

This resistance offered to the fluid flow has enhanced the pressure drop across the channel, hence a higher $f_r$ has been observed. At an angle of $\alpha = 45°$, the flow restricted by the S-shape is maximum, which leads to higher $f_r$. The effect $P/e$ of the selected S-shape turbulators on the friction factor enhancement ratio$(f_r/f_s)$ is shown in Fig. 5(b), for a range of $Re$ from 4000-16000 and keeping other geometric parameters constant viz. $e/D_h$ at 0.22 while and $\alpha$ at 30°.

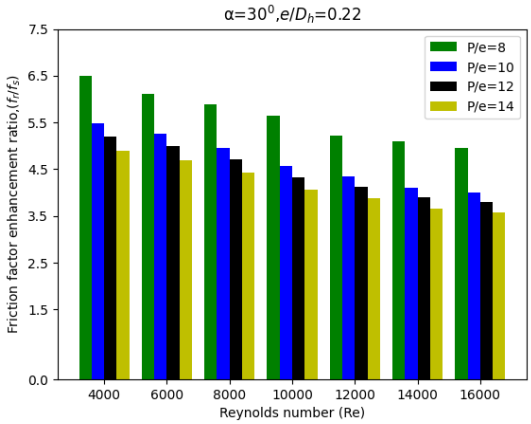


**Fig. 5(b):** Effect of $P/e$ on $f_r/f_s$

The graph demonstrates that for all values of Re, the, $f_r$ diminishes when $P/e$ increases from 8 to 14. The likely reason for maximum $f_r$ at $P/e = 8$ is that at a lower pitch, the number of turbulators rows that can be attached to the test plate is higher, and these higher numbers offer good resistance to the fluid flowing through the roughened channel. As the value of $P/e$ is increased beyond the value of 8, the number of heated elements surface decreases and thus, the resistance presented is low. The decreased number of turbulator rows attached on the test surface thus lowers the turbulent intensity, which in turn reduces $f_r$.

### 4.3 Thermo-hydraulic performance

The results reveal the effect of geometrical parameters on $Nu_r$ and $f_r$ behaviour is concluded for the S, and NACA0018 shape baffles roughened solar air passage. It has been noticed that there is a considerable rise in the $Nu_r$ by using the turbulent promoters but with a pressure drop penalty; therefore, is essential to select the geometrical parameter that enhances the heat transfer with the least possible pressure drop across the test section.

The consequence of the $\alpha$ on $\eta$ by varying the operational range of $Re$ from 4000 to 16000 is shown in Fig. 6(a) using S-shape turbulators. The graph reveals that the maximum performance has been achieved at an $\alpha$ of 30° because, at this value of $\alpha$, the heat transfer rate is extreme for the entire range of $Re$, whereas the magnitude $f_r$ is not maximum. This combined better heat transfer and the lesser pressure drop penalty helps to achieve higher thermohydraulic performance at $\alpha$ of 45° where $f_r$ is maximum, the thermohydraulic performance achieved is least. Similarly, Fig. 6(b) displays the effect of $P/e$ on $\eta$ by varying the operational range of $Re$ from 4000 to 16000. It has been noted that the supreme $\eta$ was found at $P/e$ of 12 and the minimum at $P/e$ of 14.

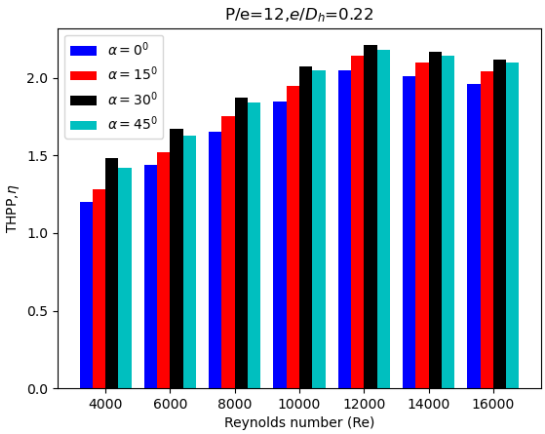


**Fig. 6(a):** Effect of $\alpha$ on $\eta$

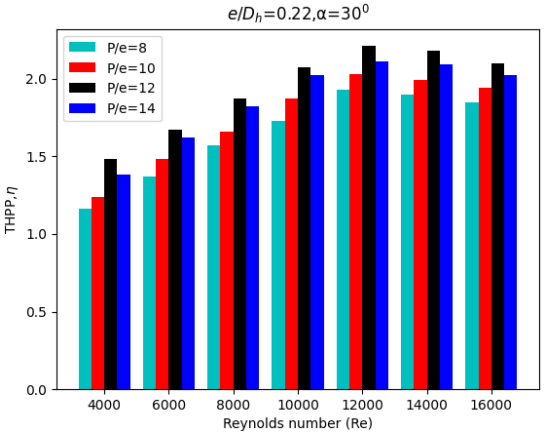


**Fig. 6(b):** Effect of $P/e$ on $\eta$

## 5. Exergetic Performance

The evaluation of the exergetic performance of a SAH channel with an artificially roughened absorber has been carried out, and the main parameter, i.e. the heated plate temperature, has been focused upon. The higher flow of air has been achieved at upper $Re$, which leads to enhanced turbulence intensity. This exergy analysis is based on second law of thermodynamics which has been used to measure the heat losses from a thermal system. Mixing fluid layers inside the channel disrupts the boundary layer and enhances air-to-absorber plate convective heat transfer. This enhanced heat transfer coefficient leads to a lower absorber plate temperature at higher $Re$. A significant reduction in the gap between the air and plate temperatures has been seen with the use of S-shape and airfoil shape turbulent promoters involved on the heated surface compared to the smooth surface.

Lower air-to-absorber temperature gradients reduce exergy losses. Minimum absorber plate temperature ($T_p$) is obtained for $P/e$ of 12 and flow angle of attack ($\alpha$) of 30° for the selected range of parameters. The solar air heater system has encountered various exergy losses, viz., optical loss ($EX_{L,Opt.}$), friction loss ($EX_{L,Fri.}$), heat transfer loss ($EX_{L,HT}$), irradiation loss ($EX_{L,Irr.}$) and the fluid heat transfer loss ($EX_{L,FHT}$). The range of measurements used in geometry that delivers the highest $Nu_r$ has been selected to represent all the exergy losses encountered, and the representation is shown in Fig. 7(a). It is reflected from the graph that the optical exergy loss ($EX_{L,Opt.}$) are constant for the entire range of $Re$, and the effect of $Re$ on optical loss is not prominent.

Likewise, the further exergy losses follow an asymptotic curve revealing no dependency on the $Re$. The rigorous analysis of exergetic performance, as presented in Fig. 7(b), indicates that the integration of S-shape and airfoil shape baffles on the absorber plate surface leads to a maximum exergetic efficiency of 2.5% for $P/e$ of 12, and $\alpha$ of 30°, at a value of $Re$ of 4000.

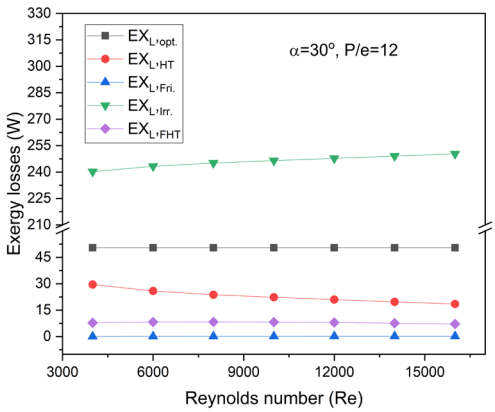


**Fig. 7(a):** Impact of $Re$ on various exergy losses

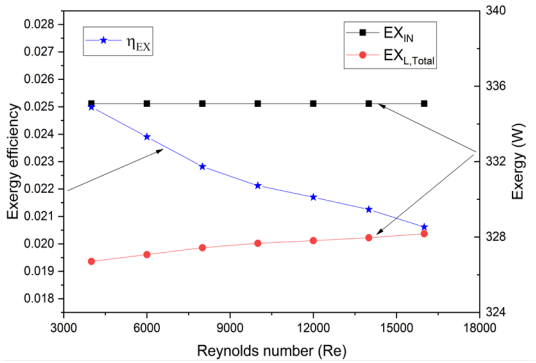


**Fig. 7(b):** Impact of $Re$ on exergy efficiency.

## 6. Conclusions

1) The performance of rectangular channel has been analyzed numerically using a combination of S and airfoil (NACA0018) shape turbulators. Three-dimensional simulations have been carried out at fixed $e/D_h = 0.22$ and by varying Re from 4000-16000, $P/e$=8-14, $\alpha$=00-450. The flowing outcomes have been inferred from the present study:
2) Turbulence zones are created near the s-shape turbulators, and fluid reattaches again near smooth NACA0018 blocks. This leads to heat transfer and friction factor enhancement.
3) The numerical results of roughened plate $Nu_r$ and $f_r$ are near to predicted results by CFD, and variations are found to be ±7% and ±5%, respectively.
4) Extreme value of $Nu_r$ is observed at P/e = 12 and $\alpha$ of 45°, while extreme value of $f_r$ is observed at P/e = 8 and $\alpha$ of 45°.
5) The attachment of turbulent promoters on the heated surface seems to be prolific as it produces the maximum $\eta$ of 2.21 at $P/e$ of 12 and $\alpha$ of 30°.
6) Exergy losses are independent of Reynolds number, and 2.25% maximum exergetic efficiency is obtained at $P/e$ =12, Re=4000 and $\alpha$=30°.

### Nomenclature

| | | | |
|---|---|---|---|
| $A$ | Absorber plate surface area ($m^2$) | $\Delta P_i$ | Pressure drop (Pascal) |
| $D_h$ | Hydraulic Dia (m) | Re | Reynolds Number |
| e | NACA0018 rib height (m) | $T_a$ | Ambient Temperature (k) |
| $e/D_h$ | Relative NACA0018 rib height | $T_p$ | Plate Temperature (k) |
| $f_s$ | Friction factor without NACA0018 rib | $T_{sa}$ | Temperature (inner duct) (k) |
| $f_r$ | Friction factor of the NACA0018 rib surface | $T_{su}$ | Sun Temperature (k) |
| H | Duct height(m) | u | Velocity ($m/s$) |
| I | Heat flux ($W/m^2$) | **Greek Symbols** | |
| k | Thermal Conductivity ($W/m.k$) | ρ | Density ($Kg/m^3$) |
| L | Duct length (m) | μ | Dynamic Viscosity($N.s/m^2$) |
| NACA | National Advisory Committee for Aeronautics | η | Thermo-hydraulic parameters |
| $Nu_s$ | Nusselt number (smooth) | $\alpha$ | Angle of attack ($^0$) |
| $Nu_r$ | Nusselt number (rib) | $\alpha_p$ | Absorptivity |
| P | Pitch (m) | $\tau_p$ | Transmissivity |
| P/e | Relative pitch | | |
| Pr | Prandtl Number | | |

### References


1) D. Jin, J. Zuo, S. Quan, S. Xu, and H. Gao, "Thermohydraulic performance of solar air heater with staggered multiple v-shaped ribs on the absorber plate," *Energy*, **127** 68–77 (2017). doi:10.1016/j.energy.2017.03.101.
2) A.S. Yadav, T. Alam, G. Gupta, R. Saxena, N.K. Gupta, K.V. Allamraju, R. Kumar, N. Sharma, A. Sharma, U. Pandey, and Y. Agrawal, "A numerical investigation of an artificially roughened solar air heater," *Energies (Basel)*, **15** (*21*) (2022). doi:10.3390/en15218045.
3) D.K. Rabha, P. Muthukumar, and C. Somayaji, "Experimental investigation of thin layer drying kinetics of ghost chilli pepper (capsicum chinense jacq.) dried in a forced convection solar tunnel dryer," *Renew Energy*, **105** 583–589 (2017). doi:10.1016/j.renene.2016.12.091.
4) S. Mghazli, M. Ouhammou, N. Hidar, L. Lahnine, A. Idlimam, and M. Mahrouz, "Drying characteristics and kinetics solar drying of moroccan rosemary leaves," *Renew Energy*, **108** 303–310 (2017). doi:10.1016/j.renene.2017.02.022.
5) A. Khanlari, A. Sözen, F. Afshari, C. Şirin, A.D. Tuncer, and A. Gungor, "Drying municipal sewage sludge with v-groove triple-pass and quadruple-pass solar air heaters along with testing of a solar absorber drying chamber," *Science of the Total Environment*, **709** (2020). doi:10.1016/j.scitotenv.2019.136198.
6) K. Kulkarni, and K.-Y. Kim, "Comparative study of solar air heater performance with various shapes and configurations of obstacles," *Heat and Mass Transfer*, **52** (*12*) 2795–2811 (2016). doi:10.1007/s00231-016-1788-3.
7) A. Standards, C. November, A. Board, and D. Janu-, "Methods of testing to determine the thermal performance of solar collectors," **1986** (*Ra 91*) (1991).
8) A.S. Yadav, and A. Sharma, "Experimental investigation on heat transfer enhancement of artificially roughened solar air heater," *Heat Transfer Engineering*, **44** (*7*) 624–637 (2023). doi:10.1080/01457632.2022.2079048.
9) A.S. Yadav, O.P. Shukla, A. Sharma, and I.A. Khan, "CFD analysis of heat transfer performance of ribbed solar air heater," *Mater Today Proc*, **62** 1413–1419 (2022). doi:https://doi.org/10.1016/j.matpr.2021.12.560.
10) V. and R.K.T. and D.M.K. Yadav Anil Singh and Shrivastava, "CFD-Based Correlation Development for Artificially Roughened Solar Air Heater," in: A. and K.S.S. and J.P.K. Kumar Anil and Pal (Ed.), Recent Advances in Mechanical Engineering,

Springer Nature Singapore, Singapore, 2021: pp. 217–226.
11) A.S. and S.N.K. and J.D. Prasad Rakesh and Yadav, "Heat Transfer and Friction Characteristics of an Artificially Roughened Solar Air Heater," in: P.M.V. and S.B.S. Saha Pankaj and Subbarao (Ed.), Advances in Fluid and Thermal Engineering, Springer Singapore, Singapore, 2019: pp. 613–626.
12) A. Singh, and S. Singh, "CFD investigation on roughness pitch variation in non-uniform cross-section transverse rib roughness on nusselt number and friction factor characteristics of solar air heater duct," *Energy*, **128** 109–127 (2017). doi:https://doi.org/10.1016/j.energy.2017.04.008.
13) M.K. Sahu, and R.K. Prasad, "Thermohydraulic performance analysis of an arc shape wire roughened solar air heater," *Renew Energy*, **108** 598–614 (2017). doi:10.1016/j.renene.2017.02.075.
14) M.K. Lalji, R.M. Sarviya, and J.L. Bhagoria, "Exergy evaluation of packed bed solar air heater," *Renewable and Sustainable Energy Reviews*, (2012). doi:10.1016/j.rser.2012.04.024.
15) S. Sharma, R.K. Das, and K. Kulkarni, "Computational and experimental assessment of solar air heater roughened with six different baffles," *Case Studies in Thermal Engineering*, **27** 101350 (2021). doi:https://doi.org/10.1016/j.csite.2021.101350.
16) S. Sharma, R.K. Das, and K. Kulkarni, "Performance Evaluation of Solar Air Heater Using Sine Wave Shape Obstacle," in: S.K. Acharya, D.P. Mishra (Eds.), Current Advances in Mechanical Engineering, Springer Singapore, 2021: pp. 541–553.
17) S. Sharma, R.K. Das, and K. Kulkarni, "Parametric optimization of solar air heater having sine wave baffles as turbulators," *Experimental Heat Transfer*, **0** (*0*) 1–26 (2022). doi:10.1080/08916152.2022.2108525.
18) A. Bekele, M. Mishra, and S. Dutta, "Effects of delta-shaped obstacles on the thermal performance of solar air heater," *Advances in Mechanical Engineering*, (2011). doi:10.1155/2011/103502.
19) K. Mohammadi, and M. Sabzpooshani, "Comprehensive performance evaluation and parametric studies of single pass solar air heater with fins and baffles attached over the absorber plate," *Energy*, **57** 741–750 (2013). doi:https://doi.org/10.1016/j.energy.2013.05.016.
20) R. Maithani, S. Sharma, and A. Kumar, "Thermo-hydraulic and exergy analysis of inclined impinging jets on absorber plate of solar air heater," *Renew Energy*, **179** 84–95 (2021). doi:https://doi.org/10.1016/j.renene.2021.07.013.
21) R. Nadda, R. Maithani, and A. Kumar, "Effect of multiple arc protrusion ribs on heat transfer and fluid flow of a circular-jet impingement solar air passage," *Chemical Engineering and Processing: Process Intensification*, **120** (*July*) 114–133 (2017). doi:10.1016/j.cep.2017.07.005.
22) M.R. Collins, and H. Abulkhair, "An evaluation of heat transfer and effectiveness for unglazed transpired solar air heaters," *Solar Energy*, (2014). doi:10.1016/j.solener.2013.11.012.
23) M. Yang, P. Wang, X. Yang, and M. Shan, "Experimental analysis on thermal performance of a solar air collector with a single pass," *Build Environ*, **56** 361–369 (2012). doi:10.1016/j.buildenv.2012.04.009.
24) R. Maithani, and J.S. Saini, "Heat transfer and friction factor correlations for a solar air heater duct roughened artificially with v-ribs with symmetrical gaps," *Exp Therm Fluid Sci*, **70** 220–227 (2016). doi:10.1016/j.expthermflusci.2015.09.010.
25) A. Kumar, R. Kumar, R. Maithani, R. Chauhan, M. Sethi, A. Kumari, S. Kumar, and S. Kumar, "Correlation development for nusselt number and friction factor of a multiple type v-pattern dimpled obstacles solar air passage," *Renew Energy*, **109** 461–479 (2017). doi:https://doi.org/10.1016/j.renene.2017.03.030.
26) R.L. Webb, and E.R.G. Eckert, "Application of rough surfaces to heat exchanger design," *Int J Heat Mass Transf*, (1972). doi:10.1016/0017-9310(72)90095-6.
27) K. Kumar, D.R. Prajapati, and S. Samir, "Heat transfer and friction factor correlations development for solar air heater duct artificially roughened with 's' shape ribs," *Exp Therm Fluid Sci*, **82** 249–261 (2017). doi:https://doi.org/10.1016/j.expthermflusci.2016.11.012.
28) D. Wang, J.J. Liu, Y. Liu, Y. Wang, B. Li, and J.J. Liu, "Evaluation of the performance of an improved solar air heater with 's' shaped ribs with gap," *Solar Energy*, **195** (*13*) 89–101 (2020). doi:10.1016/j.solener.2019.11.034.
29) N.T. Luan, N.M. Phu, N. Thanh, and N. Minh, "Thermohydraulic correlations and exergy analysis of a solar air heater duct with inclined baffles," *Case Studies in Thermal Engineering*, **21** (*May*) 100672 (2020). doi:10.1016/j.csite.2020.100672.
30) J. Hu, K. Liu, M. Guo, G. Zhang, Z. Chu, and M. Wang, "Performance improvement of baf fl e-type solar air collector based on fi rst chamber narrowing," *Renew Energy*, **135** 701–710 (2019). doi:10.1016/j.renene.2018.12.049.
31) C.E. Bensaci, A. Moummi, F.J.S. de la Flor, E.A.R. Jara, A. Rincon-Casado, and A. Ruiz-Pardo, "Numerical and experimental study of the heat transfer and hydraulic performance of solar air heaters with different baffle positions," *Renew Energy*, **155** 1231–1244 (2020). doi:10.1016/j.renene.2020.04.017.
32) F. Afshari, A. Sözen, A. Khanlari, A.D. Tuncer, and C. Şirin, "Effect of turbulator modifications on the thermal performance of cost-effective alternative solar air heater," *Renew Energy*, **158** 297–310 (2020).

doi:10.1016/j.renene.2020.05.148.
33) R. Maithani, and S. Sharma, "Thermo-hydraulic and exergetic analysis of rectangular channel with integrated jet impingement and roughness," *Experimental Heat Transfer*, **0** (*0*) 1–23 (2023). doi:10.1080/08916152.2023.2298483.
34) H. Moussaoui, K. Chatir, A.D. Tuncer, A. Khanlari, M. Kouhila, A. Idlimam, and A. Lamharrar, "Improving environmental sustainability of food waste using a solar dryer: analyzing drying kinetics and biogas production potential," *Solar Energy*, **269** 112341 (2024). doi:https://doi.org/10.1016/j.solener.2024.112341.
35) D. Jin, M. Zhang, P. Wang, and S. Xu, "Numerical investigation of heat transfer and fluid flow in a solar air heater duct with multi v-shaped ribs on the absorber plate," *Energy*, **89** 178–190 (2015). doi:10.1016/j.energy.2015.07.069.
36) I. Singh, and S. Singh, "CFD analysis of solar air heater duct having square wave profiled transverse ribs as roughness elements," *Solar Energy*, **162** (*January*) 442–453 (2018). doi:10.1016/j.solener.2018.01.019.
37) C. Sivakandhan, T. V Arjunan, and M.M. Matheswaran, "Thermohydraulic performance enhancement of a new hybrid duct solar air heater with inclined rib roughness," *Renew Energy*, **147** 2345–2357 (2020). doi:10.1016/j.renene.2019.10.007.
38) I. Singh, S. Vardhan, S. Singh, and A. Singh, "Experimental and cfd analysis of solar air heater duct roughened with multiple broken transverse ribs: a comparative study," *Solar Energy*, **188** (*February*) 519–532 (2019). doi:10.1016/j.solener.2019.06.022.
39) A.S. Yadav, and J.L. Bhagoria, "A cfd based thermo-hydraulic performance analysis of an artificially roughened solar air heater having equilateral triangular sectioned rib roughness on the absorber plate," *Int J Heat Mass Transf*, **70** 1016–1039 (2014). doi:https://doi.org/10.1016/j.ijheatmasstransfer.2013.11.074.
40) S.K. Jain, R. Misra, A. Kumar, and G. Das Agrawal, "Thermal performance investigation of a solar air heater having discrete v-shaped perforated baffles," *International Journal of Ambient Energy*, **43** (*1*) 243–251 (2022). doi:10.1080/01430750.2019.1636874.
41) Y.M. Patel, S. V Jain, and V.J. Lakhera, "Thermo-hydraulic performance analysis of a solar air heater roughened with reverse naca profile ribs national advisory committee for aeronautics," *Appl Therm Eng*, **170** (*September 2019*) 114940 (2020). doi:10.1016/j.applthermaleng.2020.114940.
42) S. Zaphar, and G. Verma, "Thermal Analysis of an Evacuated Tube Solar Collector using a One-end Stainless Steel Manifold for Air Heating Applications under Diverse Operational Conditions," 2023.
43) S. Kaushik, A. Kumar Verma, S. Singh, N. Kanojia, S. Panwar, S. Kindo, S. Uniyal, S. Goswami, D. Som, and N. Kumar Yadav, "Comparative Analysis of Fluid Flow Attributes in Rectangular Shape Micro Channel having External Rectangular Inserts with Hybrid Al 2 O 3 +ZnO+H 2 O Nano Fluid and (H 2 O) Base Fluid," 2023.
44) L.A. Rasheed, J. A-K Mohammed, and R.A. Jessam, "Performance Enhancement of a Single Pass Solar Air Heater by Adopting Wire Mesh Absorber Layer," 2023.
45) S. Kaushik, V. Uniyal, A. Kumar Verma, A. Kumar Jha, S. Joshi, M. Makhloga, P. Singh Pargai, S.K. Sharma, R. Kumar, and S. Pal, "Comparative Experimental and CFD Analysis of Fluid Flow Attributes in Mini Channel with Hybrid CuO+ZnO+H2O Nano Fluid and (H2O) Base Fluid," 2023.
46) S. Sharma, R.K. Das, and K. Kulkarni, "Performance Evaluation of Solar Air Heater Using Sine Wave Shape Obstacle," in: S.K. Acharya, D.P. Mishra (Eds.), Current Advances in Mechanical Engineering, Springer Singapore, Singapore, 2021: pp. 541–553.
47) S. Kumar, R.K. Das, and K. Kulkarni, "Comparative study of solar air heater (sah) roughened with transverse ribs of naca 0020 in forward and reverse direction," *Case Studies in Thermal Engineering*, **34** 102015 (2022). doi:https://doi.org/10.1016/j.csite.2022.102015.
48) I. Yaningsih, D. Danardono Dwi Prija Tjahjana, E. Prasetya Budiana, M. Muqoffa, Z. Arifin, K. Enoki, and T. Miyazaki, "Numerical study on the Effect of Rectangular and Triangular Counter-Rotating Vortex Generators on the H-Rotor Wind Turbine Performance," 2023.
49) V. Kumar Agrawal, and H.P. Khairnar, "Experimental & Analytical Investigation for Optimization of Disc Brake Heat Dissipation Using CFD," 2022.
50) S. Sharma, R.K. Das, and K. Kulkarni, "Performance Evaluation of Solar Air Heater Using Sine Wave Shape Obstacle," in: S.K. Acharya, D.P. Mishra (Eds.), Current Advances in Mechanical Engineering, Springer Singapore, Singapore, 2021: pp. 541–553.
51) R. Maithani, A. Kumar, and S. Sharma, "Effect of straight slot rib height on heat transfer enhancement of nanofluid flow through rectangular channel," *Mater Today Proc*, (2021). doi:https://doi.org/10.1016/j.matpr.2021.08.040.
52) K. Altfeld, W. Leiner, and M. Fiebig, "Second law optimization of flat-plate solar air heaters part i: the concept of net exergy flow and the modeling of solar air heaters," *Solar Energy*, **41** (*2*) 127–132 (1988). doi:https://doi.org/10.1016/0038-092X(88)90128-4.
53) M. Hedayatizadeh, F. Sarhaddi, A. Safavinejad, F. Ranjbar, and H. Chaji, "Exergy loss-based ef fi ciency optimization of a double-pass / glazed v-corrugated plate solar air heater," *Energy*, **94** 799–810 (2016). doi:10.1016/j.energy.2015.11.046.

54) M.M. Matheswaran, T. V. Arjunan, and D. Somasundaram, “Analytical investigation of solar air heater with jet impingement using energy and exergy analysis,” *Solar Energy*, **161** (*October 2017*) 25–37 (2018). doi:10.1016/j.solener.2017.12.036.